Design of Arrayed Micro-Structures to get Super-Hydrophobic Surface for Single Droplet and Bulk Flow Conditions

Ashish Mall, Prithvi Raj Jelia, Amit Agrawal, Ramesh K. Singh, Suhas S. Joshi
Department of Mechanical Engineering, Indian Institute of Technology Bombay
Email: ssjoshi@iitb.ac.in

Abstract: Surfaces with water contact angle greater than 150º are super-hydrophobic in nature and possess extraordinary water repelling properties. Various researches on wettability of textured surfaces in recent years have shown that texturing surfaces with micron-sized and nano-sized patterns improves their hydrophobicity to a great extent. This report aims at optimizing the dimensions of square-pillared arrayed textures to achieve maximum contact angle, and the effect on rounding the edges, and changing droplet size; together with simulation of bulk water flow through micro-channels having textured walls. Comparison has been made between smooth and textured surfaces in terms of pressure drop reduction and slip-length, in order to investigate the effects of textures on hydrophobicity. Pressure drop reductions up to 19%, obtained from simulations suggest that significant energy saving can be done in micro-fluidics using textures.

Keywords: Super-hydrophobic, microscopic textures, roughness, pressure drop, slip length

1. Introduction

A Super-hydrophobic surface is a surface for which the contact angle made by a water droplet in static equilibrium is greater than 150°. Also, they are non-wettable and self-cleaning. Lotus leaf surface is super-hydrophobic and hence the name "Lotus Effect" is sometimes given to describe the phenomenon.

Researchers are trying to fabricate super-hydrophobic surfaces by emulating the common characteristics of the naturally occurring super-hydrophobic surfaces such as the lotus leaf, to be used in a variety of industrial applications such as enhanced water proofing for fabrics, anti-contamination and lab-on-chip micro-fluidic devices such as gene delivery systems [1].We divide our work into two broad categories – (i) Static analysis of single droplet deposited over textured surface. (ii) Dynamic analysis of bulk flow over textured surface.

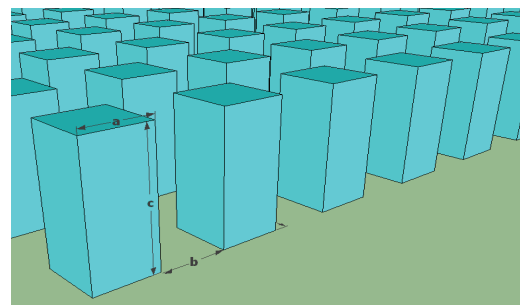## Sec I-Static Analysis of Single-Droplet

We present an analytical approach to optimize the dimensions of square pillared, square arrayed micro-structured hydrophobic surface, by considering single droplet models, to achieve maximum contact angle. Cassie-Baxter state equation predicts the apparent contact angle made by a single droplet on a textured surface as:

$$cos\theta^* = -1 + \phi\,(1 + cos\theta) \qquad (1)$$

Contrary to the predictions made by the above equation, there is a minimum value of ϕ and correspondingly maximum value of the apparent contact angle θ^*, below which decreasing the spacing ratio further, would lead to spontaneous breakdown of super-hydrophobicity [2].

2. Square Edged Pillars

We consider a hydrophobic surface textured with square arrayed square pillared microstructures (see Fig. 1).

Fig. 1 Square pillared textures arranged in an array

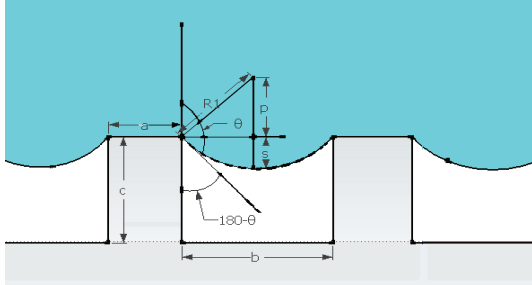The modeling and subsequent analysis is based on the following assumptions:

- The droplet is in ideal Cassie-Baxter state.
- The solid surface is hydrophobic.
- The curvature of the liquid between the pillars is convex downwards.
- The air trapped between the liquid meniscus and solid substrate is at atmospheric pressure.

- The apparent contact area (projected area) made by the droplet when deposited on the textured surface is circular in shape.
- The weight of the droplet is uniformly distributed over the apparent contact area.
- The volume of the water penetrating between the pillars is negligible

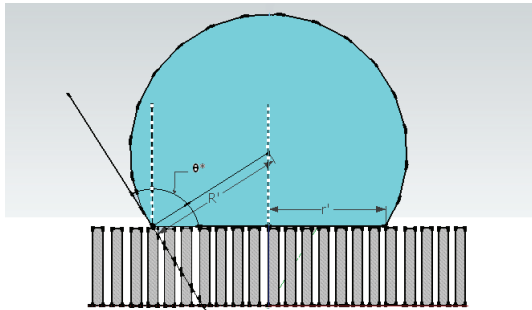## 2.1. Deriving Mathematical Constraints

2.1.1. Position where the lower meniscus touches the substrate: We know that if the lower meniscus of the droplet touches the substrate, the current Cassie-Baxter state (see Fig. 2) will be replaced by the Wenzel state [3]. To prevent the lower meniscus from touching the substrate, $s < c$, which gives,

$$\frac{c}{b} > \left(\frac{1-sin\theta}{-2cos\theta}\right) \qquad (2)$$

Fig. 2 Schematic showing side view of a droplet deposited on a textured surface

2.1.2. Weight balancing: The weight of the portion of the total droplet liquid lying above each cavity is balanced by surface tension forces arising out of the contact which liquid makes with a unit cell. r' is the radius of apparent contact area (see Fig. 3).

Fig. 3 Schematic showing a deposited droplet having spherical curvature of a different radius R'

From geometry, the apparent contact area is:

$$A = \pi R^2 sin^2\theta^* \left(\frac{4}{(1-cos\theta^*)^2(2+cos\theta^*)}\right)^{\frac{2}{3}} \qquad (3)$$

The weight of the liquid falling directly over each unit cell is given as:

$$W_1 = \frac{\rho\left(\frac{4}{3}\pi R^3\right)g}{\pi R^2 sin^2\theta^* \left(\frac{4}{(1-cos\theta^*)^2(2+cos\theta^*)}\right)^{\frac{2}{3}}}\{(a+b)^2 - a^2\} \qquad (4)$$

The surface tension force per unit cell is given as:

$$F_1 = |4aTcos\theta| \qquad (5)$$

This force should be large enough to bear the weight on each unit cell, i.e.

$$F_1 > W_1 \qquad (6)$$

2.1.3. Cassie-Baxter state is thermodynamically more stable than Wenzel state: The surface energy associated with Cassie-Baxter state should be lower than the energy associated with the Wenzel state, so that the Cassie state is thermodynamically more stable.

$$E_{w1} = \gamma_{sl}[(a+b)^2 + 4ac] \qquad (7)$$

$$E_{c1} = \gamma_{sv}[(a+b)^2 + 4ac - a^2] + \gamma_{sl}a^2 + \gamma[(a+b)^2 - a^2] \qquad (8)$$

,

$$E_{c1} < E_{w1} \qquad (9)$$

Rearranging, and using the Young's relation [4], we get,

$$cos\theta + \left(\frac{1}{1+\frac{4ac}{b^2+2ab}}\right) < 0 \qquad (10)$$

2.2. Optimization problem

Minimize $\quad f(a,b,c) = \left(\frac{a}{a+b}\right)^2$

The inequality constraints are given by Eqs. (2), (6), and (10). As a number of constants feature in constraint equations, following values were assigned to them: g = 9.81 m/sec², T = 0.072 N/m, (for water-air pair), R= 1 mm, θ = 100°, ρ = 1000 kg/m³.

2.2.1. Additional constraints: For the minimization problem some additional constraints have to be added to avoid trivial solutions and get optimum values of $\{a, b, c\}$, which are practically feasible. Also, constraints have been applied from Laser machine resolution and accuracy.

- *Avoiding Trivial Solutions:* $\{a, b, c\} > 0$
- *Practical Feasibility:* To avoid practically infeasible values, we specify an upper bound on c as, $c < c_{max}$.
- *Laser Machine Resolution:* We cannot obtain a laser beam dimension below a certain value. We have specified this as: $b > 0.01$ mm

3. Rounded Edged Pillars

Similar analysis leads to the following mathematical constraints:

- $$\frac{(c - R_c)}{b} > \left(\frac{1 - sin\theta}{-2cos\theta}\right)$$

- $$b + a <$$
$$\left(\sqrt{\begin{array}{c}\frac{-3(a - 2R_c)Tsin^2\theta^*cos\theta}{\rho Rg}\left(\frac{4}{(1 - cos\theta^*)^2(2 + cos\theta^*)}\right)^{\frac{2}{3}} \\ +(a - 2R_c)^2\end{array}}\right)$$

- $$cos\theta + \left(\frac{1}{1 + \frac{4a(c - R_c)}{b^2 + 2ab}}\right) < 0$$

Where, R_c is the radius of the rounded edges.

4. Rounded edges versus straight pillars

Energy associated with sharp-edged pillared surface per unit cell is given by Eq.(8). And the energy associated with rounded-edged pillared surface per unit cell is given as:

$$E'_{c1} = \gamma_{sl}\left[\left\{2\left(\frac{a}{2} - R_c\right)^2\right\} + \frac{2\pi R_c}{4}\{2a + 2(a - 2R_c)\}\right] + \gamma_{sv}[(a + b)^2 - a^2 + 4a(c - R_c] + \gamma[(a + b)^2 - a^2]$$

If the droplet on rounded-edged pillared surface has to be more stable, then,

$$E'_{c1} < E_{c1} \qquad (11)$$

On simplification, and substituting we get,

$$R_c > \left(\frac{\pi a}{2} - \frac{\gamma_{sv}}{\gamma_{sl}}\right) / \left(\frac{\pi - 2}{2}\right) \qquad (12)$$

Hence, the rounded-edged pillared surface leads to a more energetically favorable state compared to sharp-edged pillared surface, if the radius of the rounded corners is greater than a critical value which is dependent on the width of the pillars, a; and on the ratio of the interfacial surface tensions between solid-vapor and solid-liquid pairs.
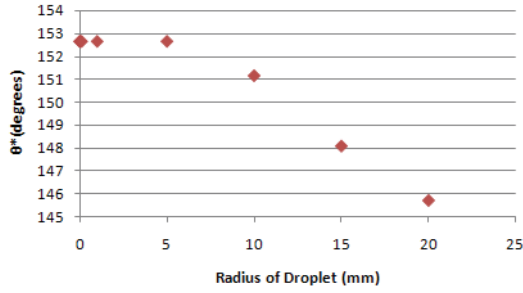
5. Results and Discussion

We solved the optimization problem using 'fmincon' solver in 'Optimtool' in Matlab.

5.1. Optimum dimensions: The optimum results from the solver are as follows: a) sharp-edged case − $\{a, b, c\} = \{0.025, 0.096, 0.991\}$mm; rounded-edged case − $\{a, b, c, R_c\} = \{0.025, 0.089, 0.0614, 0.002\}$mm. We see that the maximum attainable apparent contact angle is almost the same in both the cases. But, with sharp edges, we have to dig the surface to greater depths ($c = 991\mu$m compared with 614μm) as compared with rounded edges.

5.2 Effect of Changing Size of Droplets: As size of the droplets varies from micrometric to mill metric, effect of changing droplet size, R, was analyzed (we took $c_{max} = 0.2$mm, and carried out optimization for different values of R). It was found that, the optimum dimensions remain the same when droplet size is decreased from an initial value of 1 mm, which is the radius of droplet considered in our analysis till now. But when the droplet size is increased beyond 6 mm, the optimum dimensions for maximum super-hydrophobicity start changing. Also, as droplet size is increased, the hydrophobicity of the optimized surface goes on decreasing (see Fig. 3.8). As the capillary length, $k^{-1} = \left(\frac{T}{\rho g}\right)^{\frac{1}{2}}$, defined as the maximum droplet size for which gravitational forces are negligible compared to surface tension forces, resulting in giving the
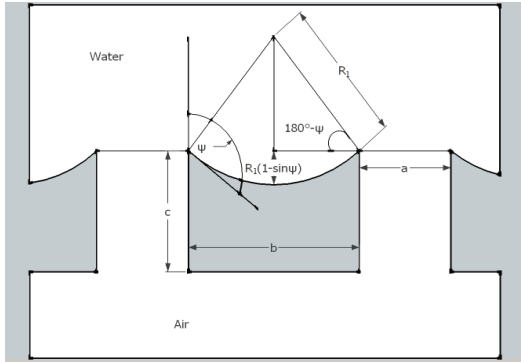
droplet a spherical cap, is of the order of 2-3 mm, we can safely assume that droplets having spherical curvature of all range of sizes, would exhibit super-hydrophobicity on the optimized surface.

Fig. 4 Apparent contact angle decreases when the radius of droplet becomes of the order of centimeters

Sec II-Dynamic Analysis of Bulk Flow

The simulations in this report involves a study of changes in surface geometry and its influence on pressure drop on the laminar bulk flow of water in microchannels whose bottom surface is textured with microgrooves.

Fig. 5. Schematic of the shear-free air-water interface

Based on the various experimental observations [5-8], it is a well known fact that when water flows in a microchannel whose surface is textured with microposts, air is trapped in between the microposts spacing. An air-water interface is formed between the microposts and supported by surface tension as shown in Fig. 5. These 'air-pockets' provide a shear-free path in the flow of water and help reduce pressure gradients necessary for flow. This can be understood by the concept of slip.
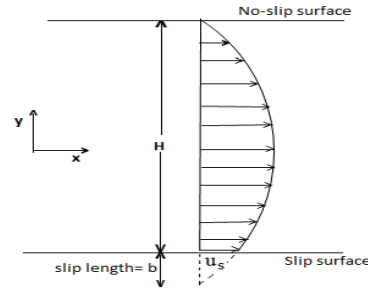
6. Liquid slip

If velocity of a flowing liquid at the wall is not zero, we say that liquid is slipping and the velocity at the wall is called slip velocity (Fig.6). Navier proposed a model in which the slip velocity at the wall u_s is proportional to the shear strain rate experienced by the wall [5, 9]

$$u_s = s(\partial u / \partial y)_{y=0} \tag{13}$$

The constant s is called slip-length.

For a fully developed steady laminar flow between two parallel plates, the Navier-Stokes equation can be written as [10]

$$\frac{dp}{dx} = \mu \frac{d^2 u}{dy^2} \tag{14}$$

Fig. 6 Liquid slip at wall

By applying the boundary conditions $u=0$ at $y=H/2$, $u=u_s$ at $y= -H/2$ and $u_s = s(\partial u/\partial y)_{y=0}$ at $y= -H/2$, the average velocity u_{avg}[5, 6] of fluid between the plates can be written as

$$u_{avg} = \frac{H^2}{4\mu}\left(-\frac{dp}{dx}\right)\left[\frac{1}{3} + \frac{s}{s+H}\right] \tag{15}$$

Here the term $(s/s+H)$ is the contribution due to slip at wall. This slip will show significant effect on flow if the slip length s is comparable to the length scale of the flow geometry (H).

7. Influence of Surface Roughness on Slip-length

It has been found experimentally that when a smooth surface is textured with patterns, its slip-length increases manifold. The main reason for the higher slip length values on textured surface is that the interfacial solid-liquid contact area is

reduced. . The air remains trapped in the cavity region. Since air exerts very little shear resistance to the liquid flow than the wall, the average velocity of the liquid increases for the textured surfaces compared to the smooth surface. Thus, the slip length is higher for the textured surfaces.

8. Influence of Surface Roughness on Pressure Drop

Recent developments in superhydrophobic surfaces have shown that a significant reduction in the frictional drag and pressure drop can be achieved for liquids flowing in microchannels with textured surfaces.

The degree of pressure drop reduction can be controlled by controlling the spacing between the microgrooves. The boundary condition for the liquid in contact with the top of microgrooves is no-slip, while the air-water interfaces supported between the microgrooves is shear-free and do not resist the flow. If the distance between the microgrooves is increased keeping the width of microgrooves constant, higher values of reduction in pressure drop can be achieved.

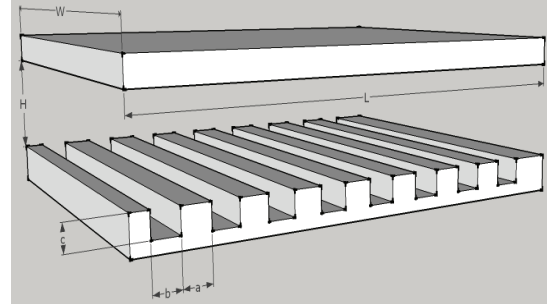## 9. Simulation of Bulk Flow on Textured Surfaces

Fig. 7 shows a schematic of the microchannel used in simulation, including some physical dimensions. The length, width and height of the microchannel are L, W and H respectively. The bottom surface of the channel is patterned with microgrooves. Width of the microgrooves is a, spacing is b and height is c.

The relationship between u_{avg} and pressure gradient for a smooth pipe where no-slip boundary condition is applied would be [10]

$$u_{avg} = \frac{H^2}{12\mu}\left(-\frac{dp}{dx}\right) \qquad (16)$$

In order to investigate the effects of textures, pressure drop values have been calculated for textured surfaces (from simulations) and compared with the pressure drop values for smooth surfaces (Eq. (16)) for the same flow velocity($V_i = u_{avg}$). Here, V_i is the uniform inlet

velocity and u_{avg} is the average velocity in fully developed region.

Fig. 7 Schematic of the microchannel including physical dimensions

10. Results and Discussion

A series of simulations were performed on smooth and patterned microchannels to investigate the effects of different parameters such as pattern spacing b, height c and channel height H on pressure drop reduction. Since the simulations are done using flow with unsteady model, the measurements were taken at t=1s for every simulation. The measurements were made at x= 1mm and beyond, where the flow is fully developed, to avoid the effects of development of velocity profiles.
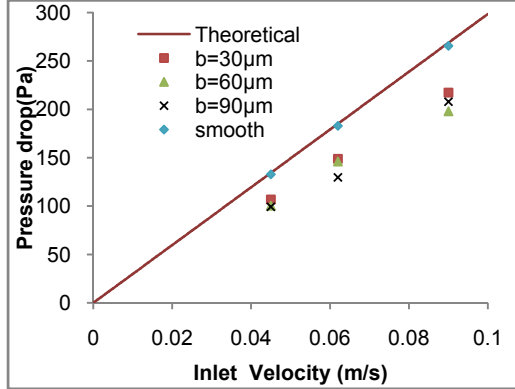
10.1. Change in Geometry

10.1.1 Change in microgroove spacing b: Fig.8 shows the pressure drop as a function of flow rate for different values of b. The continuous line is theoretical pressure drop for steady laminar flow between parallel plates, calculated by using the formula (obtained from Eq. (16))

$$-\Delta p = \frac{12u_{avg}\mu}{H^2}\Delta L \qquad (17)$$

where, Δp is the value of pressure drop across the length ΔL. ΔL=4mm is taken from x=1mm to x=5mm, where the flow is fully developed. The pressure drop values for smooth surface almost coincide with the theoretical results, which show the accuracy of the simulations.

It can be seen from Fig. 8 that, in each case, the pressure drop increases linearly with the flow rate. For all the textured surfaces, the pressure drop was found to be significantly smaller than the smooth surface and the theoretically

predicted values where no-slip boundary condition is applied to the bottom surface.

Fig. 8 Pressure drop as a function of flow velocity for different spacing

The reduction in the pressure drop values for the spacing b=90 μm are not found as per the expectation. For inlet velocity 0.045m/s, the reduction in the pressure drop for b=90 μm is very close to that for b=60 μm. This is because as width b increases the air-water interface starts touching the bottom of the cavities and the trapped air escapes from the cavities. Fig. 9 shows the air-water interface for two condition set of parameter to understand the effect of changing b.

(a)   (b)

Fig. 9 Volume fractions of air and water for $a=c$ =30μm, V_i=0.045m/s (a)b=30μm(b)b=90 μm

The maximum pressure difference at the air-water interface, which can be supported by surface tension, can be obtained by [5, 11]

$$\Delta p_i = p_w - p_a = \frac{4\gamma}{b}cos(\pi - \theta) \quad (18)$$

The effect of b on the air-water interface can be seen from Eq. (18). As b increases, the right hand side $(4\gamma/b)\,cos(\pi - \theta)$ which is the maximum pressure difference Δp_i, the microgrooves can support decreases. So it is possible that for larger values of b, the meniscus
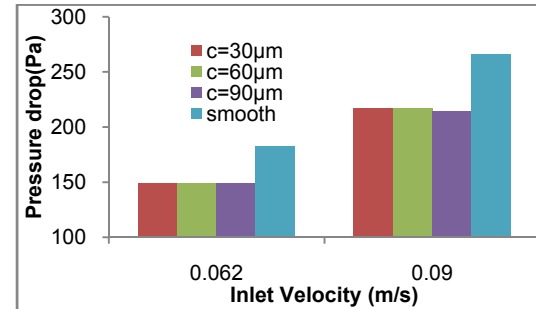
can touch the bottom surface of the grooves and hence water can fill the cavities.

The condition for the meniscus not to touch the bottom of the cavity will be

$$(b\,/\,2)cos\theta(1 - sin\theta) < h \quad (19)$$

If b is increased to a value such that Eq. (19) does not satisfy, the air-water interface starts touching the bottom of the cavities and water fills in the cavities.

11.1.2. Change in microgroove height c: To investigate the effect of microgroove height c, simulations with changing c were performed while keeping the remaining parameters constant for two different flow rates. Fig. 10 shows the pressure drop values for each simulation for comparison.
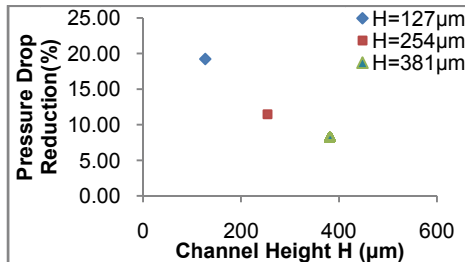

Fig. 10 Pressure drop as a function of microgroove height c for different flow rates

It can be seen from Fig. 10 that the pressure drop values, for each flow rate, are almost constant for different values of microgroove height c. The reason for the constant pressure drop is that the fractions of no-slip and slip regions are not changing; only the amount of air which is trapped between microgrooves changes.

11.1.3 Change in channel height H: The effect of the channel height on pressure drop reduction was measured for three different values of channel height H (H=127,254 and 381 μm) keeping remaining parameters fixed ($a=b$=30μm, c=90μm, $V_i=u_{avg}$=0.09 m/s). Since pressure drop also depends on channel height H apart from u_{avg} (Eq. (15)). So the percentage pressure drop reduction will be a better measure to observe the effect of channel height on pressure

drop reduction. Percentage pressure drop reduction is defined as [5, 8]

$$\rule{3cm}{0.4pt} \tag{20}$$

Fig. 11 Pressure drop as a function of microchannel height H

The reason for the decreased values of percentage pressure drop reduction for higher values of channel height H is that the ratio H/s increases (assuming that the slip length s is very small and nearly constant for a given geometry of roughness) as H is increased. As explained earlier, slip enhances the flow significantly only when slip length s is comparable to the length scale of the flow geometry (height H).

12. Conclusions

- In the case of bulk water flow through microchannels, textures improve hydrophobicity by reducing the required pressure gradients for the flow.
- The fundamental cause of improving the hydrophobicity is the trapped air in the cavities of textures, which exerts no shear to the flow.
- The advantage of textures is limited to lower pressure values in the microchannel. At higher pressure, the trapped air starts escaping from the cavities, resulting in loss of hydrophobicity.
- Increasing the fraction of shear-free area by increasing the spacing between microgrooves causes higher pressure drop reduction. But the disadvantage of large spacing is that the upper pressure limit which the texture can support decreases.
- Both straight edged and round-edged pillared textures can induce super-hydrophobicity
- Rounding of edges leads to more stability of the super-hydrophobic state, only when radius of the rounded edges is greater than a critical value.
- The optimized surface exhibits super-hydrophobicity for all range of drops of spherical curvatures.

References

1. Lin Feng, Shuhong Li, Yingshun Li, Huanjun Li, Lingjuan Zhang, Jin Zhai, Yanlin Song, Biqian Liu, Lei Jiang, and Daoben, " Super-Hydrophobic Surfaces: From Natural to Artificial," *Advanced Materials,* **24** (14) (2002), 1857-1860.
2. Rob J. Klein, P. Maarten Biesheuvel, Ben C. Yu, Carl D. Meinhart, and Fred F. Lange, " Producing Super-Hydrophobic Surfaces with Nano-Silica Spheres," *International Journal of Materials Research*, (2004), 377-380.
3. Anthony J. Schrauth, Nannaji Saka, and Nam P. Suh, "Development of Nano-Structured Hemocompatible Surfaces," *Massachusetts Institute of Technology,* (2005)
4. David Quere, "Non-sticking drops, "*Institute of Physics Publishing,* **68** (11) (2005), 2495-2532.
5. Jia Ou, Blair Perot, and Jonathan P. Rothstein, "Laminar drag reduction in microchannels using ultrahydrophobic surfaces", *Physics of Fluids*, **16** (12) (2004), 4635-4643.
6. Jia Ou and Jonathan P. Rothstein, "Direct velocity measurements of the flow past drag-reducing ultrahydrophobic surfaces", *Physics of Fluids*, **17** (10) (2005), 103606.
7. R. N. Govardhan, G. S. Srinivas, A. Asthana, and M. S. Bobji, "Time dependence of effective slip on textured hydrophobic surfaces", *Physics of Fluids*, **21** (5) (2009), 052001.
8. Peng-Fei Hao., Catherine Wong, Zhao-Hui Yao, and Ke-Qin Zhu, "Laminar Drag Reduction in Hydrophobic Microchannels", *Chemical Engineering & Technology*, **32** (6) (2009), 912-918.
9. K. Watanabe, Yanuar, and H. Udagawa, "Drag reduction of Newtonian fluid in a circular pipe with a highly water-repellent wall", *Journal of Fluid Mechanics*, **381** (1999), 225-238.
10. F.M. White, "Fluid Mechanics", *Mcgraw-Hill College, 4th Edition*, 1998.
11. J. Eijkel, "Liquid slip in micro- and nanofluidics: Recent research and its possible implications," Lab on a Chip, **7** (2007), 299-301.